CHARGED PARTICLE VETO DETECTOR FOR THE PHOS SPECTROMETER

A.M.Blick[1], **M.Yu.Bogolyubsky**[1], **A.Di Mauro**[2],
S.V.Erine[1], **C.Gregory**[2], **F.Hahn**[2], **S.Haider**[2],
M.S.Ippolitov[3], **Yu.V.Kharlov**[1], **A.Klovning**[4],
O.A.Maeland[4], **P.Martinengo**[2], **N.G.Minaev**[1],
O.H.Odland[4], **F.Piuz**[2], **R.Rongved**[4], **B.Skaali**[5],
S.A.Sadovsky[1], **V.D.Samoylenko**[1], **I.Sibiriak**[3],
V.I.Suzdalev[1], **V.V.Tikhonov**[1], **M.Volkov**[3],
J.Van Beelen[2], **D.Williams**[2], **A.Zviagine**[1]

1) *Institute for High Energy Physics, Protvino, Russia*

2) *CERN, Geneve, Switzerland*

3) *Kurchatov Institute of Atomic Energy, Moscow, Russia*

4) *Department of Physics, University of Bergen, Norway*

5) *Department of Physics, University of Oslo, Norway*

Abstract

The general design of the Charged Particle Veto (CPV) detector for the photon spectrometer (PHOS) of the ALICE experiment along with beam test results of the CPV prototype in 1998 are presented.

1 Introduction

1.1 CPV layout

The Charged-Particle Veto (CPV) detector is designed to suppress detection of charged particles hitting the front surface of the PHOS. The CPV consists of four separate modules, each of them placed on top of one PHOS module. In Fig. 1 the integration of the PHOS and the CPV into the ALICE setup is shown. The physical requirements on
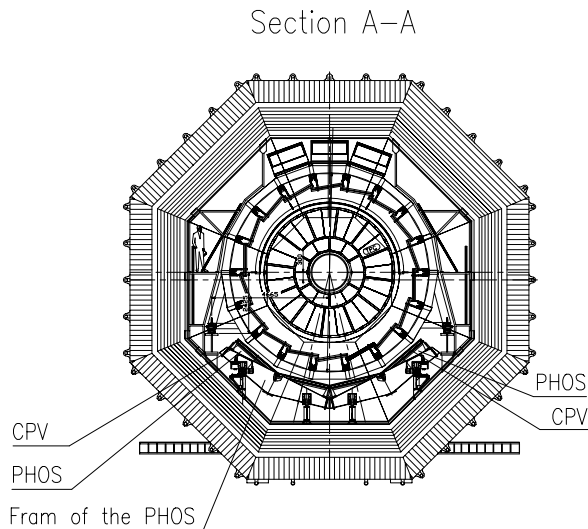

Figure 1: Common integration of the PHOS and CPV into the ALICE setup.

the CPV are the following:

- large-area modules of $\sim 230 \times 200$ cm^2,
- high detection efficiency for charged particles, close to 100%,
- two dimensional readout with localization accuracy of 3 mm,
- minimum amount of material, less than 5% of X_0, electronics included,
- minimum dead-zone,
- low neutron sensitivity.

The detector based on the MWPC with pad readout and Ar/CO$_2$ gas mixture fulfills all the above requirements. In particular due to the absence of hydrogen in the operating gas the CPV will have low sensitivity to neutron fluxes. A similar detector is also used for the HMPID RICH, see [1].

The CPV modules are positioned at approximately 5 mm upstream of the PHOS modules, Fig. 2. In offline charged particle hits in the veto planes are projected onto the PHOS modules, and for each hit the corresponding region in the PHOS is marked as affected by charged particle. The showers in the PHOS with coordinates in these regions will be then rejected as produced by charged particles.

1.2 Trigger capabilities of the CPV

The CPV can also provide an interesting possibility for the PHOS calibration with cosmic muons. This calibration procedure makes use of the trigger capability of the CPV and of the special L3 muon counter [2] installed in the top of L3 magnet. Cosmic muon calibration would be very useful between physical runs at LHC because there is no other possibility for the PHOS calibration that time.

Trigger capabilities of the CPV are based on the wire readout. If one includes in coincidence the OR signal from all CPV wires with the L3 signal one could select
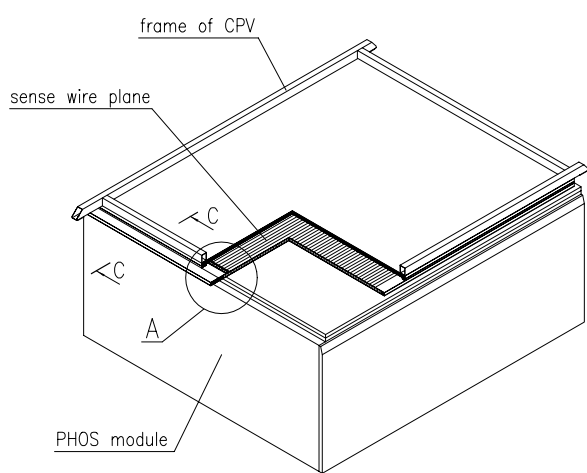
Figure 2: General layout of the PHOS and CPV detectors.

cosmic muons which are going within angles of $\pm 15^o$ compared to the normal CPV plane directions. Thus the selected muons are going mainly through one or two neighboring crystals and muon signals in the PHOS will be therefore well detectable.

The intensity of the charged penetrating component of cosmic rays crossing a horizontal area is $0.8 \times 10^2 \ m^{-2} s^{-1} \ sterad^{-1} s$, at sea level. The muon rate for one PHOS module will be of the order of $50 \ s^{-1}$. The average energy in the PHOS from one MIP particles is of order 250 MeV, thus one needs 5-10 days for the full PHOS calibration.
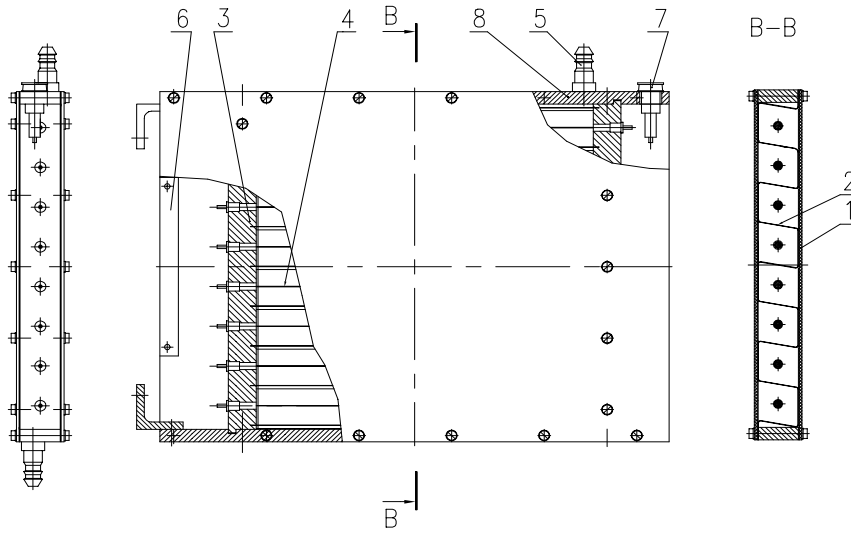
2   CPV Prototype

2.1   Construction of the CPV prototype

The prototype of the CPV detector was designed and produced during summer — autumn of 1998. Low-mass construction materials were used for the production to minimize radiation length, material budget and detector weight. It was made as a plane structure with dimensions 18×18 cm^2 filled with eight proportional tubes equipped with cathode pad readout based on the GASSIPLEX chip as front-end electronics, for details see the engineering design in Fig. 3. The key element of the CPV construction is lithographically produced pad cathode. 0.8 mm thick cooper-clad G10 foils was used to form the cathodes of proportional tubes, the outer and inner cooper cladding play role of the detector electromagnetic shield and cathode sheet with a fine pad structure. Transversal (relative to the anode wires of prototype) cross section of each tube is rhombus shaped with small deviation from a square, in order to improve spatial resolution in the direction transversal to the anode wires. The wire pitch is 2.2 cm. The cathode pad sizes, 2.2×2.2 cm^2, are the same as the transversal dimensions of the scintillating crystals in the PHOS. The other main parameters of CPV prototype are as follows:

- anode wires have diameter 50 μm and made of gold-plated tungsten with 3% renium,
- anode-cathode distance is $D = 1.1$ cm,
- work gas mixture as 80% Ar + 20% CO_2.

2.2   Results of the CPV Prototype Tests

The tests of the CPV prototype were performed in September-October 1998 at the T10 and T11 beam lines (CERN, accelerator PS) in a wide range of incident momenta $(1-10)$ GeV/c of beams of different charged particles (electrons, muons and hadrons). The experimental equipment of these beam lines included the system of scintillating counters (for triggering and selection of beam particles) as well as coordinate detectors: 10 planes

2

CPV prototype: 1—PCB with pads; 2—folded Al—foil;
3—endcup; 4—W+Au wire; 5—gas inlet;
6—read out connector; 7—HV connector;
8—wall.

Figure 3: The CPV prototype.

of Microstrip Silicon Detectors (MSD) with strip pitch 50 μm and aperture 2×2 cm^2 at channel T10 and scintillating hodoscope (SH) with 1 mm plastic sticks and aperture 6.4×6.4 cm^2 at channel T11.

For tests the CPV prototype was placed in the beams with normal orientation of its plane with respect to the beam particles propagation, so that the anode wires were lying horizontally along X-axis. Vertically oriented Y-axis was directed across the wires.

During irradiation of the CPV prototype by charged particles signals from the cathode pads were amplified by GASSIPLEX chips, transferred to the ADC's in an experimental barrack and finally stored on the DAQ computer disc in digital form.

2.2.1 Amplitude spectra and Clusters

Analysis of the experimental data shows that the pad signals from a single minimum ionization charged particle normally crossing the CPV plane are grouped into clusters elongated in the horizontal direction (along the wires). Fig. 4 presents the typical amplitude spectra of the pad signals at High Voltage (HV) of 2050 V. In Fig. 4a, particular, the spectrum for the pad with maximal amplitude (main pad) in the cluster is shown, and in Fig. 4b the spectrum for the adjacent pads (relatively to the main one) is also shown.

The cluster size N (in pad numbers) changes mainly from one to three with negligible contamination of the longer clusters. The average part of clusters with given value of N in total sample depends essentially on the high voltage applied to the CPV. Fig. 5 presents cluster size distribution in number of pads along the anode wires at fixed high voltage 2050 V, and dependence of the contribution ϵ_{XN} of the clusters with given N in the total sample on the high voltage applied.

From the last figure one can conclude that relative part of clusters with size $N > 1$
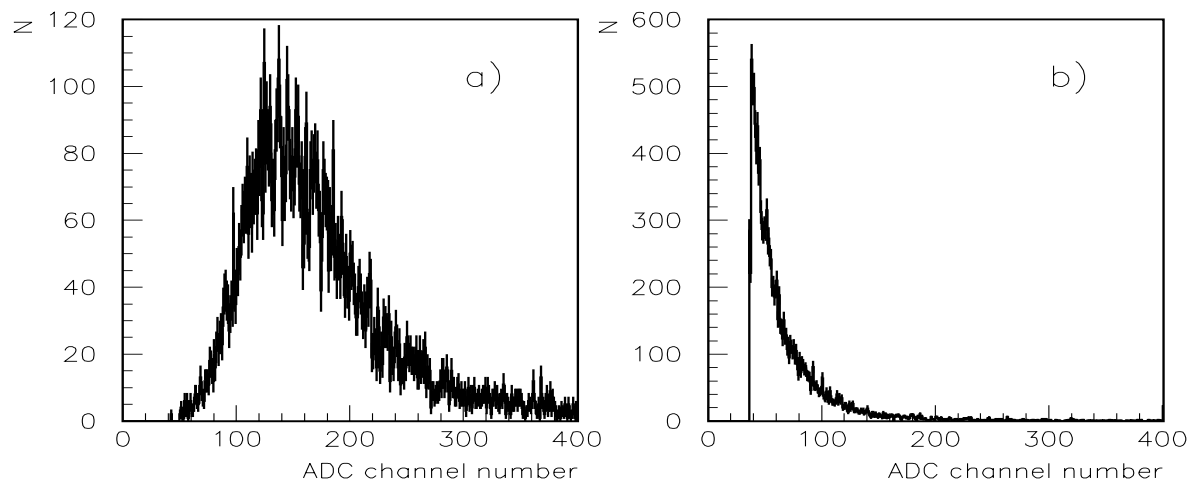
3

Figure 4: Amplitude spectra of the signals from the CPV cathode pads. Part (a) of the figure presents the results for the main pad with maximal amplitude in the cluster elongated along anode wire direction, the part (b) shows the analogous distribution for neighboring pads (relatively main pad) in the same cluster. High voltage is 2050 V.

increases with the high voltage, and, for example, the contamination of one-pad clusters is less than 4% at 2050 V.
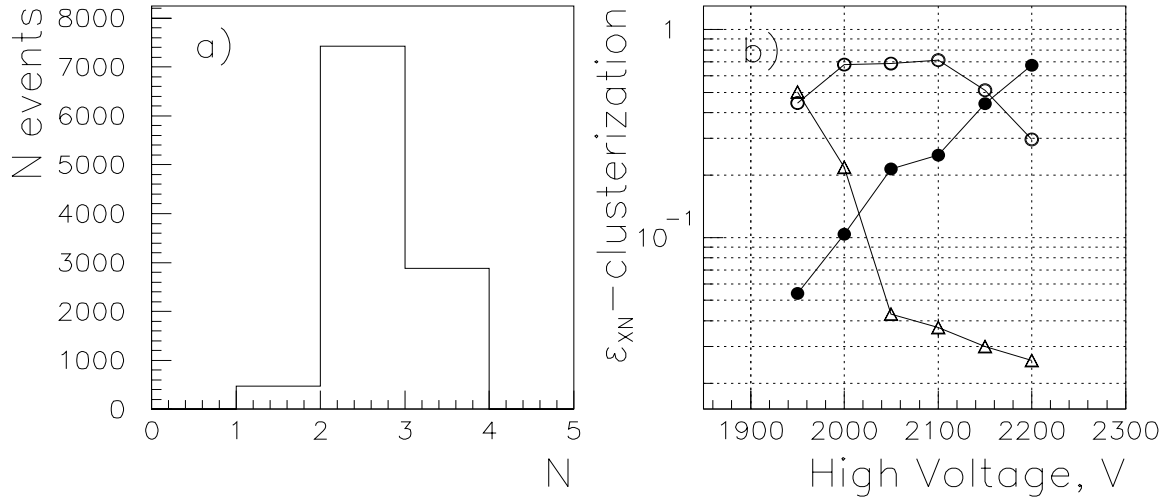

Figure 5: Cluster size distribution in pad numbers N along the wire direction at high voltage 2050 V (a), and dependence of the contribution ϵ_{XN} of the clusters with given N into the total sample on the high voltage applied (b); here triangles, white points and black points represent data for clusters with $N = 1$, $N = 2$ and $N = 3$ respectively.

2.2.2 Charged Particles Detection Efficiency

Another important characteristic of the CPV is detection efficiency for charged particles. We have measured the CPV efficiency for prototype using the MSD detectors, the results are presented in Fig. 6 as function of the high voltage applied. The efficiency ϵ demonstrate character behaviour for MWPC: it increases together with growth of the high voltage in region $1950 - 2000$ V, and then, at higher voltage values, it has an approximate plateau. On this plateau, for example at 2050 V, the efficiency $\epsilon \simeq 0.99 \pm 0.016$, that is quite resonable for such kinds of detectors.
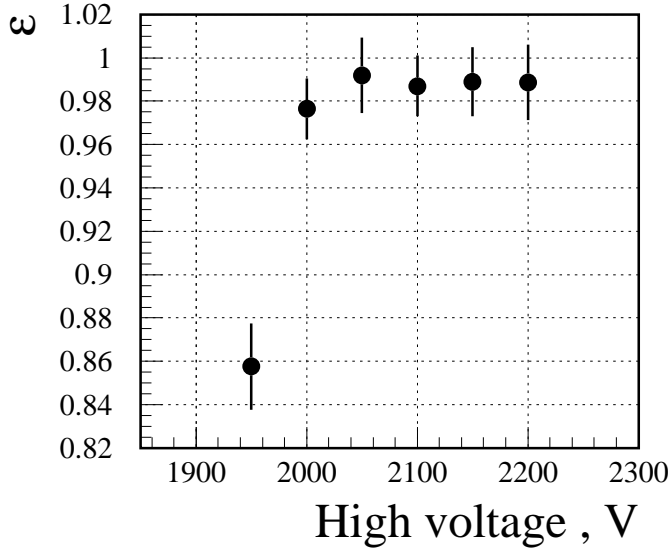
4

Figure 6: Charged particle detection efficiency in the CPV prototype as function of the high voltage applied.

2.2.3 Cathode Charge Density Distribution and Cumulative Function

The induced charge density distribution $\phi(x')$ on the CPV pads can be defined from experimental data taking into account proportionality of the signals from pads to the charge collected on its surfaces. The Charge Cumulative function $F(x')$ for charged particle crossing the CPV in point $x'_0 = 0$ is defined as follows:

$$F(x') = \int_{-\infty}^{x'} \phi(x'')dx'' \ . \tag{1}$$

with the normalization $F(x' = \infty) = 1$. Here and below we use undimensional normalized coordinate x' as well as pad side size a':

$$x' = x/D \ , \qquad a' = a/D, \tag{2}$$

where D is anode-cathode distance.

If we numerate pads in a cluster along the wires by index n the signal A_n from each pad in the cluster can be easy expressed through the function $F(x')$:

$$A_n = K \cdot [F(na' + a'/2 - x') - F(na' - a'/2 - x')] \ . \tag{3}$$

where K is coefficient of proportionality for charge-amplitude transferring. Because the coordinates x' were measured by the MSD the last equation can be used for determination of the Cumulative function from the experimental dependence of the amplitudes in pads on the x'. For fit of the experimental distributions we used three different approximations for charge density distribution $\phi(x')$ [1, 3, 4]:

$$\phi(x') = \alpha/\cosh(\beta x') \ . \tag{4}$$

$$\phi(x') = (\beta/\pi)/(x'^2 + \beta^2) \ . \tag{5}$$

$$\phi(x') = \alpha \cdot \frac{1 - \tanh^2(\beta x')}{1 + \gamma \cdot \tanh^2(\beta x')} \ . \tag{6}$$

5

Table 1: Results of the fit of experimental data for different Charge Cumulative functions.

Approximation	α	β	γ	χ^2/Np
(4)	0.248±0.003	0.829±0.003	—	21.6/36
(5)	—	0.915±0.003	—	20.1/36
(6)	0.284±0.004	0.277±0.008	6.95±0.76	16.2/36

and correspondent Cumulative functions. Formula (4) follows from the analysis of electrostatic anode charge reflection which induces the cathode charge distribution in the case of the open geometry of detector [4]. Expression (5) determines $\phi(x')$ as Cauchy function, that can simplify following calculations because they can be performed in analytical form in this case. And finally, expression (6) is often considered as the most general approximation of the charge density on pads, see [1] and additional references therein.

All three functions mentioned above describe the experimental data well, see Table 1. The best description is obtained with general and more complicated function (6). Nevertheless simple approximation (5) works also quite well. The curve in Fig. 7a presents extracted from the experiment shape of the Charge Cumulative function according to charge density (5). Additionally in Fig. 7b function (5) itself is also shown.
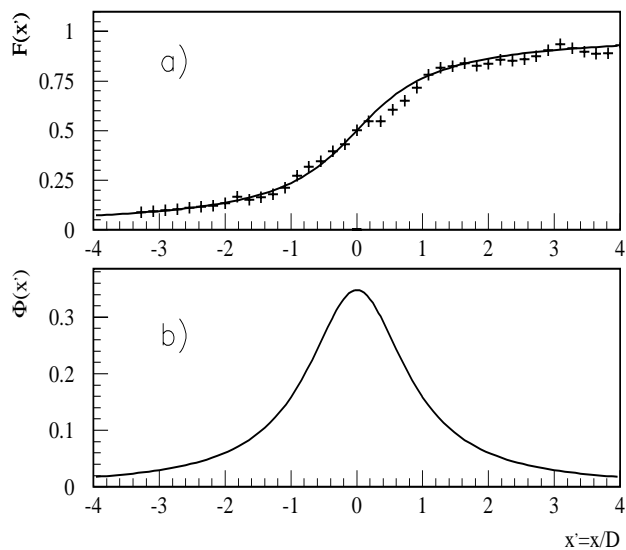

Figure 7: Experimental shape of the Charge Cumulative function in dependence on the normalized coordinate x' together with the fit accordingly to formula (5) shown with solid curve (a), and cathode charge density distribution corresponding to this fit (b). The high voltage is 2050 V.

2.2.4 Pad Response Function of the CPV prototype

The Cumulative function gives ability to calculate charge induced on pads by charged particle crossing the CPV. This charge is usually expressed in terms of the Pad Response function $P(x')$, which determines the part of total induced charge collected on a pad in dependence on hit coordinate in the CPV. Thus from formula (1) one immediately obtains

$$P(x' - x'_c) = F(x'_c - x' + a'/2) - F(x'_c - x' - a'/2) , \qquad (7)$$

where x'_c is the normalized coordinate of the pad center.

This general expression can be essentially simplified, if approximation (5) for charge

density function will be used. As result we have

$$P(x' - x'_c) = \frac{1}{\pi} \cdot [\ \arctan(\frac{x'_c - x' + a'/2}{\beta}) - \arctan(\frac{x'_c - x' - a'/2}{\beta})\ ]\ . \tag{8}$$

From this it follows that for central hit ($x' = 0$) the main pad ($x'_c = 0$) and each of two lateral ones ($x'_c = \pm a$) collect respectively 52% and 14% of the total induced charge. In the case of hit close to the edge of the main pad ($x' \simeq \pm a'/2$) two pads collect about identical parts of charge 37% each, and the third lateral one collects only $\sim$6%, more details see in Fig. 8.
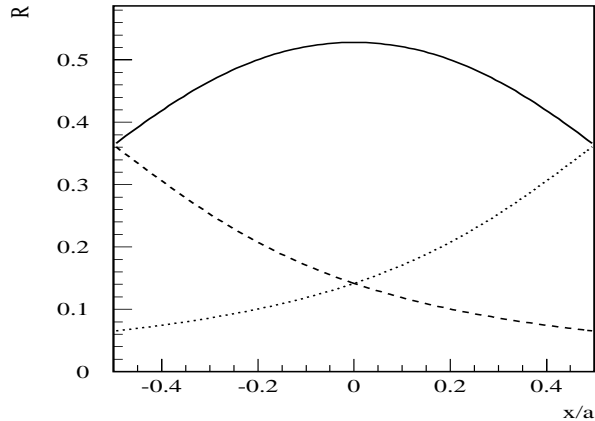

Figure 8: Fraction R of the total charge in the main cluster pad in dependence on undimensional hit coordinate x/a obtained for charge density approximation (5) with parameters from Table (1) (solid curve) and the same fractions for lateral left and right pads (dashed and dotted curves respectively). The high voltage is 2050 V.

In Fig. 9 average amplitude for the main pad in cluster ($x'_c = 0$) is presented in dependence on the hit x'-coordinate. The approximation (8) provides good description of the data (dashed curve in Fig. 9 in the region of central pad ($|x'| < a'/2$) with parameter β from Table 1. A rather good approximation of the Pad Response function can be obtained also by Gaussian, which is shown by solid curve in the figure. The correspondent fitted value of width is equal to
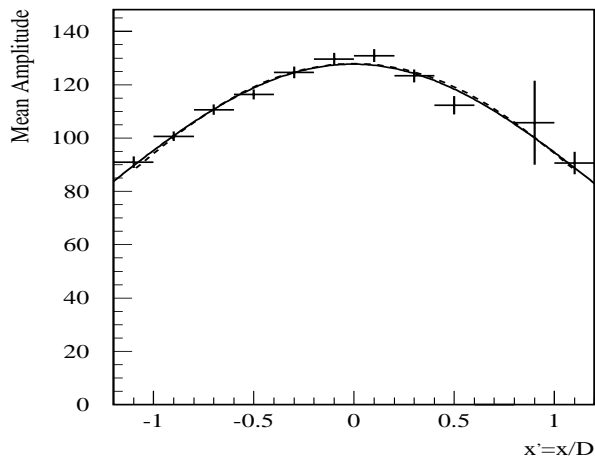
$$\sigma' = 1.15 \pm 0.05\ . \tag{9}$$

Figure 9: Dependence of the average amplitude from the main pad of cluster on x'-coordinate of hit in the coordinate system with origin in centre of the same pad. Solid curve presents fit with Gaussian, while dashed curve demonstrates the description of data by function (8) with parameter β from Table 1. The high voltage is 2050 V.

2.2.5 CPV Spatial Resolution

Really a good spatial resolution (essentially better than $a/\sqrt{12}$, where a is pad side size along x-direction) can be achieved only for 2- and 3-point clusters with using of special weighting procedure of the detected signals. The problems arising here were carefully analysed in work [4], where a simple formula was proposed to calculate measured

coordinate Δx relatively of the cluster geometrical center. This formula was obtained for 3-points clusters with an assumption about Gaussian shape of the Pad Response function

$$\Delta x = \frac{a}{2} \cdot \frac{\ln(A_1/A_{-1})}{\ln(A_0^2) - \ln(A_1 \cdot A_{-1})} \ , \tag{10}$$

where a is pad side size in x-direction and A_n (with $n = 0, \pm 1$) are pad signals in the analysed cluster. We can improve the cited formula by adding parameters α_3 and β_3, which allow one to take into account some deviation from the Gaussian and also to introduce the proper small corrections due to not ideal relative channel calibration. In result, the level of accuracy is 20%–30% better compared with using of (10). The formula has form

$$\Delta x = \frac{a}{2} \cdot [\alpha_3 \cdot \frac{\ln(A_1/A_{-1})}{\ln(A_0^2) - \ln(A_1 \cdot A_{-1})} + \beta_3] \ . \tag{11}$$

We found that $\alpha_3 = 1.15$, $\beta_3 = -0.05$, i.e. the parameters are close to unity and zero respectively. The optimal values of these parameters are not changed practically in our high voltage work region $1950\ V - 2200\ V$, excluding the only α_3 which falls to $\alpha_3 = 1.0$ at the high voltage value of $2200\ V$.

For 2-pad cluster analogous formula can be also obtained. Elementary consideration shows that in assumption of Gaussian behaviour of the Pad Response function one comes to the equation

$$\Delta x = n \cdot \frac{\sigma^2}{a} \ln(A_n/A_0) \ , \tag{12}$$

where index $n = \pm 1$ is related to one of lateral pad in cluster, the main pad is labeled as usually with index 0, σ^2 is dispersion of the Gaussian approximation of Pad Response function. It can be estimated through (9) as $\sigma = D \cdot \sigma'$.

Nevertheless we found that somewhat better results (approximately on 20%–30%) in the case of 2-pad clusters are achieved by a simple weighting of logarithms of the pad signals with additional parameters α_2 and β_2. Thus for 2-pad clusters we used the following formula to calculate Δx

$$\Delta x = \frac{na}{2} \cdot [\ \alpha_2 \frac{\ln(A_n/A_0)}{\ln(A_n \cdot A_0)} \ + \beta_2] \ . \tag{13}$$

We determined the values of above introduced parameters as $\alpha_2 = 6.0$, $\beta_2 = -0.2$ and found that they do not change with the high voltage in the region from $1950\ V$ up to 2150 V. But we redefined these parameters at the high voltage value of $2200\ V$ where they are equal to $\alpha_2 = 4.5$ and $\beta_2 = -0.12$.

For 2-pad clusters the x-coordinate of the avalanche along the CPV wire is determined by the ratio of amplitudes from a pair of adjacent pads. The statistical error of the coordinate along the x direction is given then by equation:

$$\sigma_x^{theor} \simeq \frac{\sigma^2}{a} \left(\frac{\sigma_{A_n}^2}{A_n^2} + \frac{\sigma_{A_0}^2}{A_0^2} \right)^{\frac{1}{2}} \ . \tag{14}$$

For numerical estimation let us assume that for central hits in a pad the ratio σ_{A_0}/A_0 is equal to 0.05. The best spacial resolution is achieved when tracks cross the CPV strictly between two pads: $\sigma_x^{theor} = 0.072$ cm. In the worst case, i.e. when the tracks cross the centre of pad, the resolution $\sigma_x^{theor} = 0.3$ cm. But in the last case the cluster will be

8

actually 3-pad one and using 3-pad formula one obtains the increase of resolution up to 0.13 cm about.

In a real experiment the spatial resolution of tracks along the wires depends on a number of factors: mainly on inclination of the tracks and noise level of the readout electronics. The inclined tracks tend to increase of the PRF dispersion and therefore increase σ_x. The influence of the other factors: Lorentz angle, diffusion, statistic of primary ionization, gas gain fluctuation are small in our case.

Described procedure was used for reconstruction of the x-coordinates of charged particle hits in the CPV. The analysis of the experimental data shows approximately the same level of accuracy provided by both formulas, (13) and (11), used for coordinate calculations of 2- and 3-pad clusters respectively. Fig. 10 shows a scatter plot of the true (as measured with the Microstrip Silicon Detector) vs. reconstructed x-coordinate and also the distribution of the difference between them at 2050 V. A Gaussian fit to the latter distribution gives $\sigma_x = 0.125$ cm. Because the MSD strip pitch is 50 μm the resolution σ_x is mainly defined by the CPV detector.
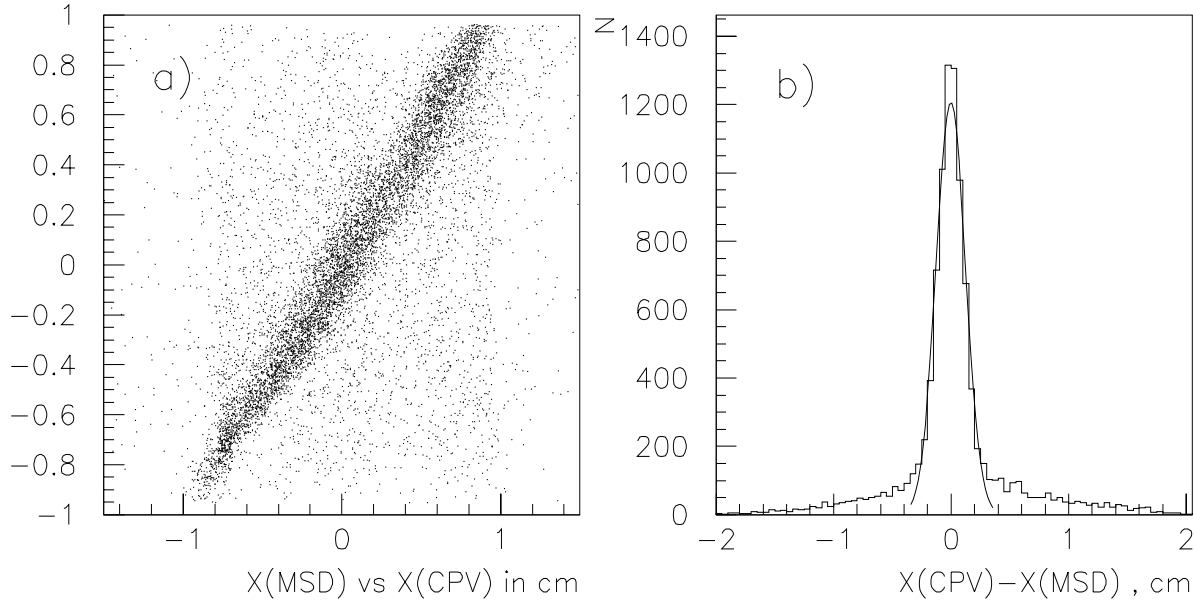

Figure 10: Correlation between measured X-coordinates of the hits for charged particles in the CPV and in the Microstrip Silicon Detector (MSD) (a), and distribution of the difference between x-coordinate determined in the CPV and in the MSD (b); solid curve represents fit of the experimental data by Gaussian corresponding to the found value of $\sigma_x = 0.125$ cm. High voltage is 2050 V.

Fig. 11 shows dependence of the CPV spatial resolution σ_x on x-coordinate of hit defined relatively to the geometrical centre of pad. One can conclude therefore that the worst spatial resolution is observed in the centre of pad, it improves closer to the pad edge.

Fig. 12 presents dependence of the CPV spatial resolution σ_x on the high voltage applied. It demonstrates character behaviour with the increase of the high voltage applied. In the region (1950 V – 2000V) σ_x decreases comparatively rapidly, whereas in the region (2000 V – 2200 V) the accuracy improves only a little and clear plateau is observed with some minor tendency of a growth at the high voltage of 2200 V.
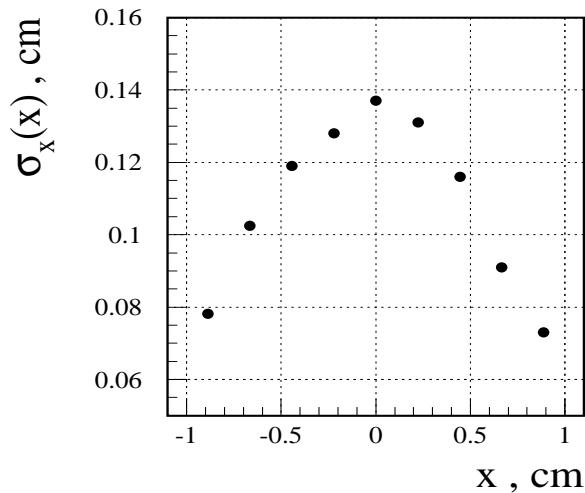
Figure 11: Dependence of the CPV spatial resolution σ_x on x-coordinate of the charged particle hit on the pad plane. Here the local system coordinate is used with origin in the geometrical centre of the analysed pad. High voltage is 2050 V.
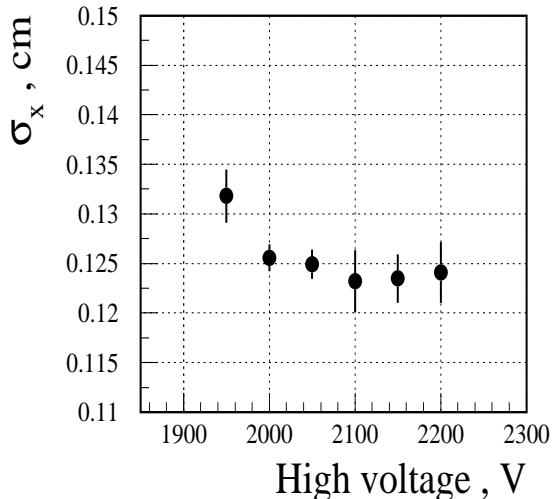

Figure 12: Dependence of the CPV spatial resolution σ_x on high voltage applied.

And finally we note that achieved level of spatial resolution was obtained actually with one wire and three pads (due to narrow beam) and therefore in a real experiment one should expect an additional distortion of the coordinate resolution due to variation of gas gain from wire to wire as well as due to natural variation of the pad and detector geometry.

2.2.6 Spatial resolution for Y-coordinate

The tested CPV prototype possesses an excellent spatial resolution for x-coordinate (along wires) and normal flux of incident charged particles compared to the CPV plane. Spatial resolution for y-coordinate (across wires) is defined by the wire pitch b accordingly to the formula $b/\sqrt{12}$. In the case of $b = 2.2$ cm one obtains $\sigma_y \simeq 0.64$ cm. In fig. 13 is shown the distribution of the differences between the true (MSD) and reconstructed y-coordinates. The dispersion of the distribution is in quite good agreement with the above mentioned expectation.

3 Charged Particle Veto Detector

3.1 Principles of operation

The CPV module is a multiwire proportional chamber with cathode pad readout. Its schematic diagram is shown in Fig. 14. The anode wires are oriented along the direction
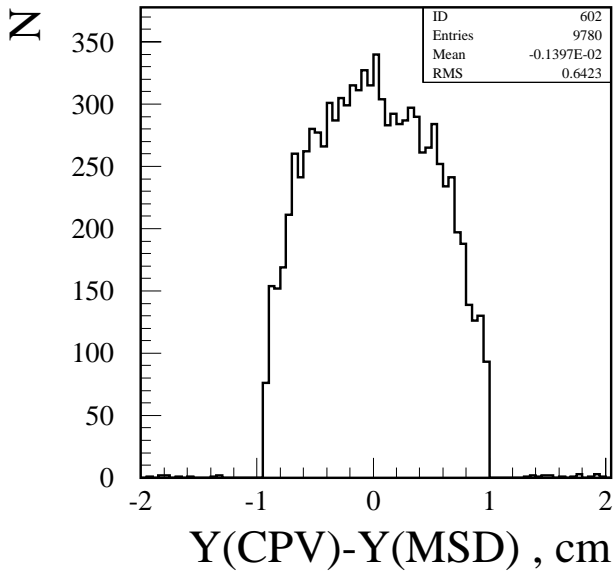
10

N

Y(CPV)-Y(MSD) , cm

Figure 13: Distribution of the difference between y-coordinate determined in the CPV and MSD. High voltage is 2050 V.

of the magnetic field in the ALICE. The wire diameter is 30 μm. The MWPC geometry is chosen as follows: the wire pitch is 5.5 mm, the cathode-anode gap is 5 mm, and the size of cathode pads is 22 $\times$ 11 mm^2 (22 mm along wires and 11 mm across wires). Gas mixture is 80% Ar+20% CO_2.
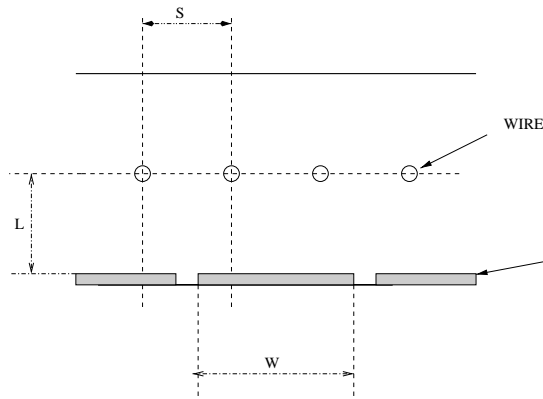

Figure 14: Schematic diagram of the CPV.

One MIP going through the gas gap of the CPV produces in average $\sim$100 electrons. The modest (less 20%) variation in the chamber gas gain does not increase essentially a dispersion of the charge induced by avalanches at the corresponding sense wires affected by the track. Two-dimensional readout is achieved by segmenting one of the printed-circuit layers (PCB) into pads and detecting the charge induced on the adjacent pads by avalanches. The Pad Response Function (PRF) relates the pad charge with the position of the avalanches relative to the pad center. The width of the PRF is a key point for the spatial resolution of two tracks in the CPV as well as for the precision of coordinate measurements of the tracks.

3.1.1 Pad Response Function

Charge collected by a pad after passing of charged particle is usually presented in terms of the pad response function. The pad response function can be expressed through the charge density distribution $\sigma(z,y)$ on one plate of the parallel-plate condenser induced by a pointlike charge Q sitting on anode wire at origin of coordinate system, i.e at point

11

with coordinates $z_Q = y_Q = 0$. This formula is as follows :

$$P(z,y) = \int_{\frac{-W_y}{2}+y}^{\frac{W_y}{2}+y} \int_{\frac{-W_z}{2}+z}^{\frac{W_z}{2}+z} \sigma(z',y') \, dz' \, dy', \tag{15}$$

where z, y denote coordinates of the pad centre along and across the wires respectively relative to the avalanche position and, W_z and W_y are the pad dimensions in these directions. In the electrostatics the exact expression for the $\sigma(z,y)$ exists [4, 5]:

$$\sigma(z,y) = \frac{-Q}{4\pi} \sum_{n=-\infty}^{\infty} \left(\frac{d\,(4\,n+1)}{\left(d^2\,(4\,n+1)^2 + z^2 + y^2\right)^{\frac{3}{2}}} - \frac{d\,(4\,n-1)}{\left(d^2\,(4\,n-1)^2 + z^2 + y^2\right)^{\frac{3}{2}}} \right), \tag{16}$$

where d is the distance between pad plate and anode wire. For our choice of the CPV parameters the calculated PRF, $P(z,0)$ and $P(0,y)$, are shown on Fig. 15 for unit value of $Q = 1$. Actually the shape of these functions is close to a Gaussian curve.
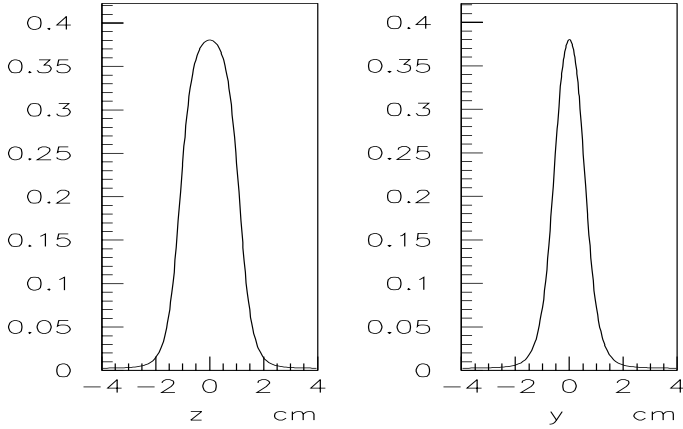

Figure 15: Pad Response Function: P(z,0) - left, P(0,y) - right.

3.1.2 Spatial resolution of the CPV

A simple consideration with assumption of Gaussian dependence of PRF on z shows that the z-coordinate of the avalanche along the CPV wire is determined by the ratio of the amplitudes P_i and P_{i+1} from a pair of adjacent pads

$$z_m = \frac{\sigma_{zPRF}^2}{W_z} \ln\left(\frac{P_{i+1}}{P_i}\right) + \frac{z_i + z_{i+1}}{2} , \tag{17}$$

where σ_{zPRF} (1.1 cm) is the width of the PRF and W_z is the pad pitch along wire direction. The statistical error of the contribution of a single wire to the coordinate measurement along z direction is then as follows:

$$\sigma_{z_m} \simeq \frac{\sigma_{zPRF}^2}{W_z} \left(\frac{\sigma_{P_{i+1}}^2}{P_{i+1}^2} + \frac{\sigma_{P_i}^2}{P_i^2} \right)^{\frac{1}{2}} . \tag{18}$$

The best resolution is achieved when a track crosses the CPV strictly between two pads. If one assume a signal-to-noise ratio of 0.05 the calculated resolution will be σ_{z_m} =0.1 cm. In the worst case, where the straight track crosses the centre of a pad, the resolution

deteriorates to 0.45 cm. But if three pad formula will be used, one can improve this resolution approximately to 0.2 cm.

In real experiment the spatial resolution of a track along the wire direction depends on a number of factors. Mainly, they originate from inclined tracks and noise of readout electronics. The inclined tracks with angle α tend to increase of the σ_{zPRF} by adding $d \cdot \tan(\alpha)/\sqrt{12}$ term and therefore increase σ_{x_m}. The influence of the other factors: Lorentz angle, diffusion, statistic of primary ionization, gas gain fluctuation are small in our case.

3.2 Mechanical design and construction

3.2.1 CPV design

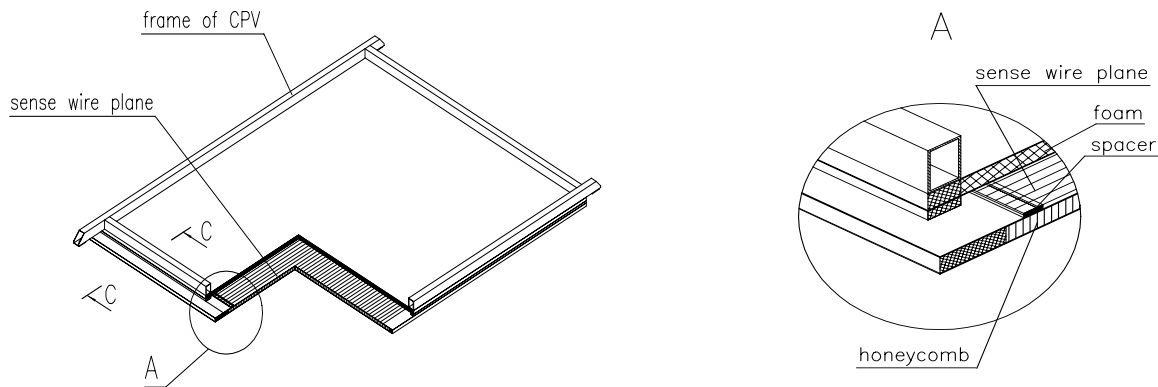The common view of the CPV detector is shown in Fig. 16. Low-mass construction

Figure 16: Common view of the CPV detector for one PHOS module (pad readout electronics is not shown).

materials will be used for the CPV production to minimize the material budget and detector weight. Each module of CPV consists of two flat rigid panels. One of which (in the top) is made of 20 mm thick sheet of foam and of two 0.8 mm thick cooper-clad G10 foils. The outer cooper cladding plays role of the detector electromagnetic shield. The inner cooper cladding forms the cathode. The cathode sheet has a fine pad structure. Schematically the pad plate is shown in Fig. 17.
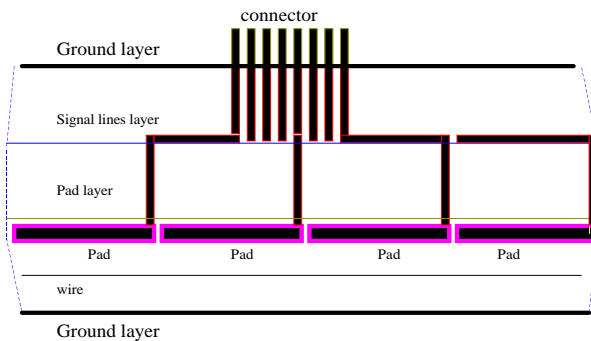

Figure 17: Cutoff view of the CPV cathode plates showing schematically pad connections.

The other panel (in bottom) is a composite type structure (cooper-clad G10 foil, nomex hexel honeycomb) inserted in a metallic frame. This technology is selected in order to provide a stiff structure of the panel with a minimum of material.

The general CPV structure is shown in Fig.18. The CPV consists of the pad PCB with Kapton circuits spaced by 20 mm thick foam plate from another circuit referred to as the ground PCB. Kapton foils are soldered on the pad PCB in rows, leaving a free space of about 20 mm between them for placing foam strips of that width. The grooves thus formed allow the Kapton foils to come out through apertures created in the ground PCB. Signals from the pads are transferred via these Kapton cable to the electronic read-out board located on the top chamber panel.

Below the pad plate there is the anode wire plane. The anode wires are made of gold-plated tungsten with 3% renium. The wire diameter is equal to 30 μm. A pitch between anode wires is achieved with precise spacer glued on the bottom cathode plane. In order to pass over the frame region, the wire trace is enclosed between two G10 foils of 1 mm thickness ensuring HV insulation. Outside the chamber at each end of the anode wires, traces are pulled in groups of eight to a well-insulated flat connector. On one side of the chamber the special PCB is used to make the HV distribution. A rubber gasket between two adjacent planes provides the gas seal for the assembly.
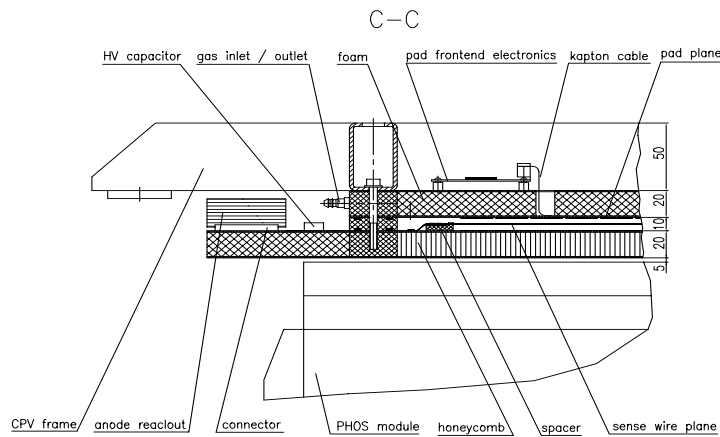

Figure 18: Cutoff view of the CPV module showing construction details.

3.2.2 Assembling procedure

The key elements in construction of the CPV are the lithographically produced pad cathode and the board with readout electronics located on the other side of the cathode plane. The other important element of the CPV construction is layout for the anode wires fixation, which includes anode wire supports of machinable ceramic Macor and support lines in the middle of modules. These support lines are made from wire coated with slightly conductive surface.

Assembly of the CPV module will be performed on a granite table. The first of cathodes is placed face down on the table. The honeycomb sheet is epoxied to the cathode. During the epoxy curing time, the honeycomb is pressed on the cathode with a simple vacuum frame.

The pad PCB is glued to the frame on a granite table and then the necessary ground connections are made with conductive glue. After this, the elements are stacked and glued together under proper load, keeping the PCB pads in contact with granite table. A flatness of ± 50 μm is achieved at area of $\sim 60 \times 60$ cm^2. The ground of the PCB makes good grounded electromagnetic shielding. The pins necessary for plugging of the FEE boards are implemented in the last queue.

14

Figure 19: Overall view of the gas system.

3.3.1 Pressure Regulation and Mixing Unit.

A standard LHC gas mixing unit is proposed. A three way valve is incorporated into each supply line which will allow a small volume of gas to flow via the exhaust for purging purposes. See Fig. 20.

The flow of component gases are metered by mass flow controllers, which have an absolute precision of 0.3% in constant conditions. Flows are monitored by a process

Figure 20: Gas mixer unit.

3.3.2 Gas Analysis

The quality of Argon and Carbon Dioxide as supplied from the CERN stores is considered adequate as far as impurities are concerned. Sampling points can be incorporated into the distribution system for the on-line measurement of oxygen and moisture in the incoming gases.

On the distribution rack sampling points on the return gas flow from each of the four Modules will monitor gas for impurities of oxygen and moisture.

3.3.3 Flow Distribution.

Final pressure regulation and flow distribution to the four Modules will take place in the shielding plug area. Gas arriving from the surface building will pass through a pressure regulator, before being distributed and passing through individual throttle valves, Fig. 21. A safety relief device is incorporated into the manifold to prevent over pressure of the Modules, this device will either be a simple relief valve or a rupture disc depending on the pressure limits.

Differential flow meters are integrated into the flow and return lines which will allow easy adjustment of individual channel flows using the throttle valves.

The bubbler oil levels at the outlet will allow to maintain the module pressure between 1 and 2 mbar above atmospheric pressure.

To prevent excess stressing of the Modules due to fluctuations in atmospheric pressure in case of a loss of the primary gas supply, a system of back filling with argon gas is proposed. This allows to fill or ballast gas to keep the Modules at bubbler pressure. Since gas is fed in near to the exhaust outlet no dilution of the module gas will occur.

16

Figure 21: Schematics of the gas distribution system.

Table 3: Main piping parameters.

	No.	Dia.	Length
SG2-Distribution	1	22/20	90 m
Distribution-Module	4	10/8	75 m
Module-Exhaust	4	16/14	75 m
Phos-Purge	4	10/8	75 m

3.3.4 Distribution Pipework.

All tubes, valves and fittings within the system will be made of Stainless Steel. Existing gas pipes at point 2 will be re-used as far as possible. Table 3 shows an overall view of the main piping parameters. At the shielding plug end they will be modified to link up with the new position of the distribution rack. In the Experimental Area (UX25) they will be extended into the L3 Solenoid Magnet, and onto the PHOS module. A patch panel, equipped with self sealing quick connectors will allow disconnection for removal of the modules.

3.4   Electronics

Low interaction rate in ALICE allows to use electronics scheme with the following specific features:

- a charge-sensitive preamplifier with large shaping time > 800 ns,
- analog charge measurements,
- multiplexed operation (MPX).

To achieve sub-millimetric accuracy of charged particle localization we are planning to use for pad readout the HPMID electronics designed to satisfy to the system requirements specific to the ALICE operational modes:

- maximum trigger interaction rates of 10 kHz and 100kHz in ion and proton collider modes respectively,

- an implementation on the detectors with a surface density of 16 kchannel/m^2.

The adopted multiplexed analog schematic is composed of two parts:

- an analog part based on the CMOS VLSI front-end chip GASSIPLEX, providing 16 analog multiplexed channels,

- a digital part performing the digitization and synchronized zero suppression.

3.4.1 Front-end chip GASSIPLEX and its operation

The 16-channel GASSIPLEX chip is composed of several function blocks per channel (see Fig. 3.15 from [1]) a charge sensitive amplifier (CSA), a switchable filter (SF), a shaping amplifier (SH) and a Track/Hold stage (T/H). The measured performances of the GASSIPLEX 1.5 and 0.7 μm versions are shown in the Table 3.8 from [1].

The GASSIPLEX is an ungated, asynchronous device, which means that its inputs/outputs are always sensitive. Therefore, when the T/H signal is set, each output is raised at constant DC level. Measuring the fluctuation of the pedestal level gives the noise figure of this channel (in practice, as the r.m.s. of a pedestal distribution). Calling PED(i) and SIG(i) the average and r.m.s. values of pedestal distribution, the operating threshold of the channel (i) is defined as:

$$TH(i) = PED(i) + N * SIG(i) ,$$

where N is a selectable constant, usually ≥ 3.

This procedure has the essential advantage of attributing the correct threshold value to every channel, regardless of the gain, noise figure and pedestal spreads among the channels and is, in fact, the prime reason to have chosen analog-based operation.

In order to exploit correctly physics data, the basic state of the system, i.e. the pedestal and noise tables of all channels, must be known, and their stability should be under control. This operation is referred to a 'pedestal run' providing the necessary pedestal and threshold tables which are stored in the memories of the digitizer/zero suppressor modules. The pedestal distributions are recorded with a pulse generator as the trigger, in the absence of any other detector signal.

At ALICE, the detectors are irradiated in a DC-mode for periods lasting a few tens of hours without beam interruption. At low interaction rates, pedestal runs could be taken in interaction mode but as few times as possible, implying a good stability of the pedestal values between measurements, i.e. in a way similar to be used in the case of HMPID [1].

3.4.2 MultiChip Module

In order to satisfy to the trigger and data flow rates expected in pp and Pb-Pb operational modes at ALICE, the final electronic system will be organized in serial/parallel architecture based on a modular array composed of three GASSIPLEX chips (48 channels), and a MultiChip Module (MCM) composed of one ADC and one zero-suppressor chip, referred to as DILOGIC. The analog part will be still implemented at the back of pad panels, while the multiplexed analog signals will be now propagated in parallel on a bus PCB to the frame of the module where the MCMs are concentrated on a motherboard. The data transfer to the DAQ is achieved by a serial optical link, see Fig. 3.34 on p.124 from [1].

The data-transfer system of the CPV will be included in the HPMID data-system. This system will consist of a single Front-End Digital Crate (FEDC) including four readout-receiver boards (RORC) and one local Data Concentrator. This crate will also contain the RORCs of the CPV detector. A standard computer is also included in the system.

3.4.3 Anode readout and trigger capabilities of the CPV

The anode readout can be used for trigger on cosmic muons for PHOS cell calibration during the operation stage of the ALICE. This is the only exclusive possibility of the PHOS calibration between LHC runs. The total number of the anode channel per one

Table 4: Electronics for the CPV pad readout.

ASIC chips:	
GASSIPLEX-0.7-1	4576
DILOGIC-1	1528
Cards and Boards:	
3-GASSIPLEX card	1528
MCM processor card	308
Column bus card	156
CMRW protocol card	1528
Power/slow control board	16

CPV module is equal to 352. The OR signals from anode wires in each CPV module in coincidence with signal from scintillation counter in the top of the ALICE setup will be used for triggering of the pads readout. The anode readout system similar to PCOS-III can be used [7].

3.4.4 Building of the CPV Electronics

The CPV electronics contains of 73216 readout channels for pads and 1408 for wires. The 3-GASSIPLEX cards (48 channels) are mounted on the ground PCB. The analog output signals transfer through Kapton cables to 8 power/slow control boards, Fig. 22. The total amount of components for the pad readout are shown in Table 4
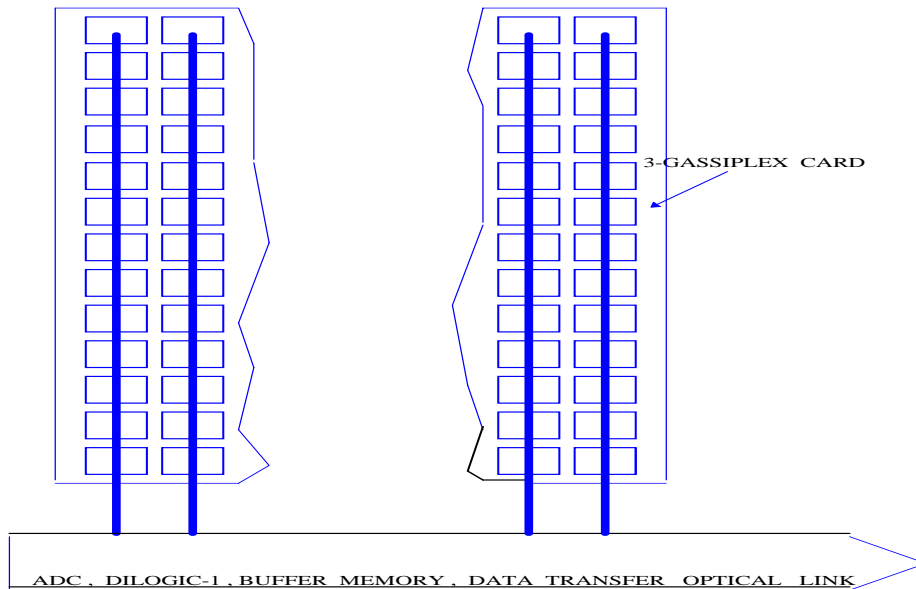
Figure 22: Schematic cable communications between electronics units for the pad readout in one CPV module.

4 CPV performance

4.1 CPV simulation model

In Chapter 2 we have discussed in detail the beam tests of CPV prototype. The obtained results alow one to formulate and tune a realistic simulation model of the CPV detector. The model is based on the pad response function (7) which parameterization was obtained in terms of the charge cumulative function (1) and charge density function (5) measured in the beam tests, see Table 1. Thus the charge density induced in a real experiment on pad plate can be calculated for any pointlike charge located near the CPV wires.

Apart from this the CPV model takes into account effects of inclined tracks in the CPV, which lead to distortion of the avalanche charge along wires and even sharing the produced charge between several wires in the case of hits with large inclined angles which especially often appear due to the track curvature in the ALICE magnetic field. Another important effect adopted in the model is the overlapping CPV clusters for neighboring charged tracks at small distances. The ground for these effect simulation is provided by the additivity principle for charge density on pads induced by avalanche charges from different tracks. For example, the charge distortion along the wires for inclined tracks is evaluated numerically by integration of the correspondent charge density along the wires.

The other important parameter of the CPV model, value of equivalent electronic noise in the CPV channels, was chosen in such manner that coordinate resolution along the wires for single normally hitted tracks will be the same as it was measured in the beam tests of CPV prototype (≈ 1.3 mm). Thus the model is virtually fixed.

4.2 Charged track reconstruction

Reconstruction procedure of CPV hits includes several steps:
- search clusters among the CPV pads with amplitudes A_i above some threshold, $A_i > A_{thr}$;
- identification of the single hit clusters and determination of the hit coordinates using formula (10) and (12);
- unfolding of the overlapping hits in clusters and determination of each hit amplitude and coordinates;
- suppression of the low amplitude hits ($A^{hit} > A_{thr}^{hit}$) and recombination of the neighboring hits into one at small distances;
- projection of the CPV hits on the PHOS crystal plane.

The hits unfolding in a cluster is based on the comparison of observed amplitude distribution in the pads with those expected in the cluster for single- or multi-particle hits. In the last case one uses the additivity principle for amplitude calculation in the pads affected by several particles. As for the expected amplitude distribution in pads for a single particle hit with arbitrary incident angles in the CPV we use the pad response function corresponded to charge cumulative function (5) obtained in the beam tests for charged particles with zero incident angles, see Table 1 for the function parameters. The χ^2 criteria is used then for unfolding the track multiplicity in such clusters.

The reconstruction program was tuned for a sample of Monte Carlo events in magnetic field of 0.2 T with charged particle flux 90 $/m^2$ expected in the ALICE for central collisions. The generated events were tracked through the real detector medium by the GALICE package. The CPV response was recorded and reconstructed. Fig.23 shows the event distribution over the number of CPV pads flushing in one CPV module ($A_i > A_{thr}$),
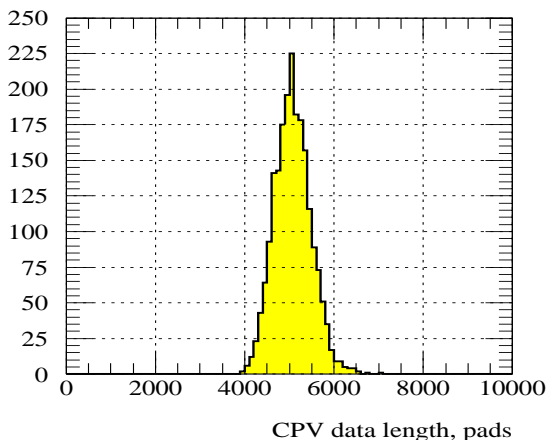
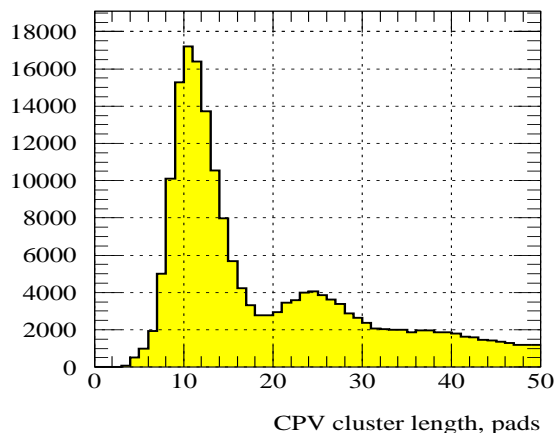Figure 23: Number of active CPV channels per module.

Figure 24: Cluster size in the CPV.

whereas Fig.24 shows the cluster size distribution in the CPV. Having in mind that the total pad number in the CPV module is equal to ~ 18000, one may estimate that CPV pad occupancy is of the order of 30%. The sizes of single hit clusters and double hit clusters are equal in average 12 and 24 pads respectively, which means that actually double hit clusters as a rule have only weak overlapping.
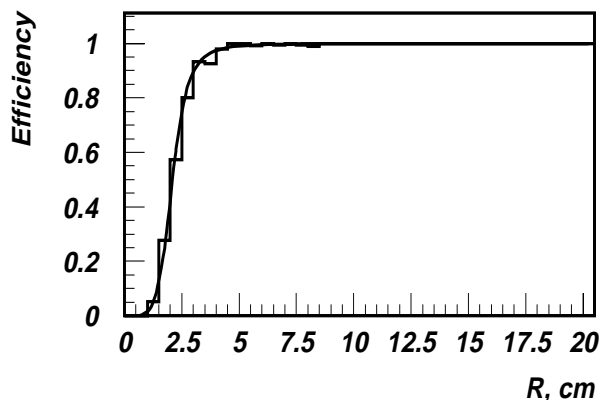

Figure 25: Unfolding efficiency for two hits in the CPV as function of the distance between them, solid line shows a smoothing function.

As for the quality of event reconstruction in the CPV, it is illustrated by Figures 25-28. In particular, the unfolding efficiency for two hit clusters is rather perfect, see Fig. 25. Actually the tracks at distances grater than 2.5 cm (remind one, that transverse size of one PHOS crystal is 2.2 cm) are resolved with probability better than 80%.

The CPV occupancy (30%) as well as cluster sizes (12 pads per single hit cluster) discussed above are sufficiently large, see Fig. 23 and 24. Such tuning of the CPV reconstruction program was made to provide high unfolding efficiency of the program for inclined tracks. Nevertheless this is rather flexible point: the occupancy and cluster sizes can be reduced several (2-3) times by increasing the amplitude threshold A_{thr} used in the reconstruction program for cluster search. But in this case the detection and unfolding efficiencies for inclined tracks as well as the coordinate resolution of the tracks would be a bit worse compared with the case of program tuning with small value of the A_{thr}. In a real experiment more fine tuning of the CPV reconstruction program will be performed

on the bases of experimental event set and achieved noise level in pads.

The present tuning of the reconstruction program provides very high detection efficiency for charged particles in the CPV. The reconstructed CPV multiplicity is shown in Fig.26, whereas in Fig.27 the deviation of reconstructed hit multiplicity from the generated one is presented. Taking into account that average CPV multiplicity in central events is 1500 hits about (see Fig.26) one can obtain that CPV multiplicity in central collisions can be reconstructed with the accuracy better than 3%.
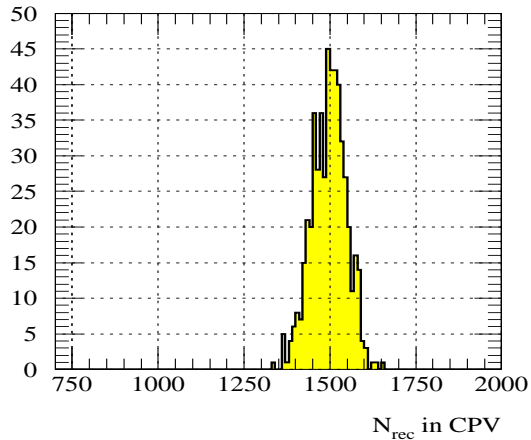
Figure 26: Multiplicity of reconstructed hits in the CPV.
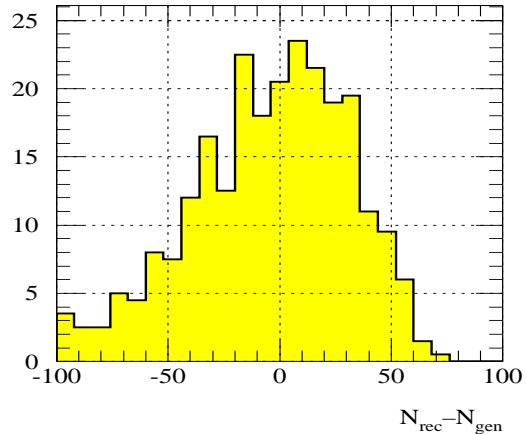
Figure 27: Deviation of the reconstructed hit number N_{rec} from generated one N_{gen} in the CPV for central Pb-Pb collisions.

And finally, a remark about the coordinate precision expected for the hit reconstruction in real experiment conditions. For so large multiplicities in the CPV modules (~ 400 hits per one module) the direct correspondence between the generated and reconstructed hits is definitely lost, nevertheless the distance from the generated hit to the closest reconstructed one can be used instead of it. The correspondent distributions over the Z (along wires) and Y (across wires) coordinate differences are shown in Fig.28 for the simulated event sample. Thus for real experimental conditions in central ion collisions we expect that the accuracy of coordinate measurements of hits will be of the order of 3 mm along and of 4.5 mm across the CPV wires respectively. These numbers take into account the track inclinations, clusters overlapping, electronics noise and influence of unfolding procedure.

4.3   Photon detection

Detection efficiency of photons in the CPV itself is rather weak. Nevertheless due to photon conversion or Compton scattering in the detectors placed between the interaction point and CPV (mainly ITS and TPC detectors) $\sim 20\%$ of the photons are accompanied by electrons (positrons) and therefore will be detected in the CPV. This effect is confirmed by direct MC simulations of the events with only photons in initial stage. As for the coordinate resolution (differences of the hit coordinates in CPV and shower coordinates in PHOS) it is equal to ~ 5 mm along and ~ 20 mm across the wires, see Fig. 29.
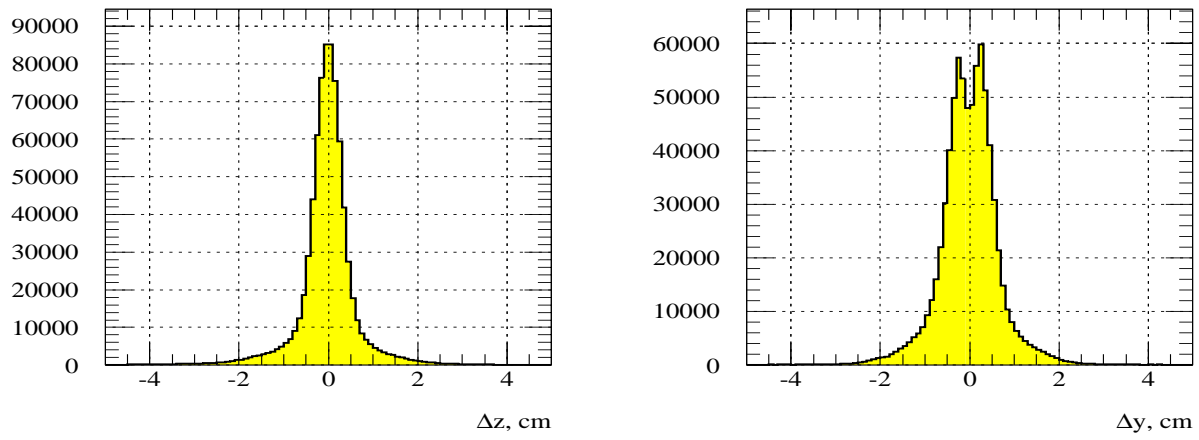
Figure 28: Resolution of Z (along wires, $\sigma \sim 3~mm$) and Y (across wires, $\sigma \sim 4.5~mm$) coordinate reconstruction of charged particles in the CPV for the simulated event sample.
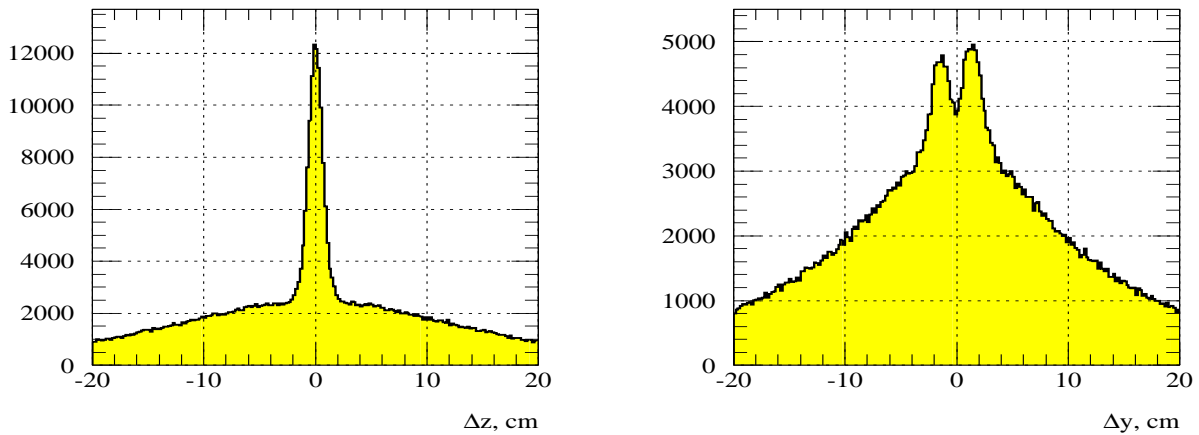

Figure 29: Coordinate differences for photons in the PHOS and the nearest hit in the CPV for events with only decay photons in the initial stage: along (left) and across (right) the wires.

4.4   Genuine photon selection

4.4.1   Charged particle showers in the PHOS

Although the PHOS is not intended for detection of charged particles and its coordinate measurement, GALICE based MC-simulations definitely show that detection possibilities for charged hadrons in the PHOS are quite satisfactory although $\sim 65\%$ of hadrons produce in the PHOS a signal just equivalent to one MIP. Even in this worst case the coordinate resolution for the hadrons is defined by the PHOS crystal size and equal to $2.2~cm/\sqrt{12} \sim 0.64~cm$. In a general case this can be illustrated by Fig. 30, 31, where the difference of exact coordinates on the CPV plane and reconstructed coordinates in the PHOS for 0.5 and 1 GeV/c charged pions are presented. The observed shift in the Y-coordinate (across magnetic field) is caused by an inclination of charged tracks in the magnetic field. To correct for this shift it would be useful to know the inclination of the tracks in the CPV.
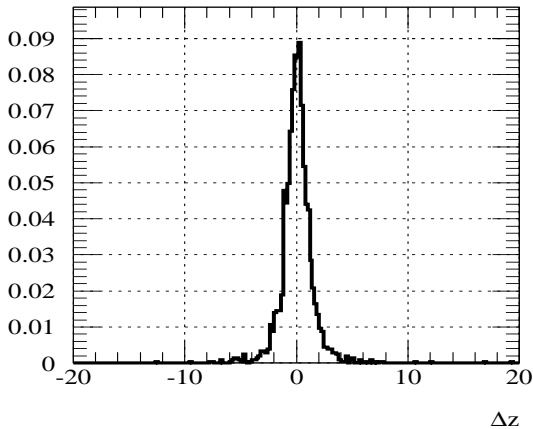
Figure 30: Difference in cm between exact π^--coordinate in the CPV plane and the shower coordinate in the PHOS along magnetic field, B=0.2 T.
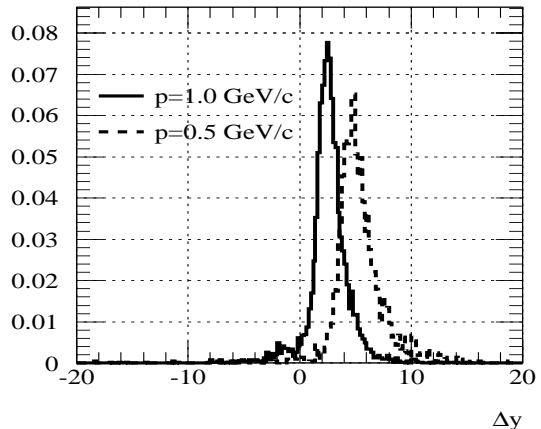
Figure 31: Difference in cm between exact π^--coordinate in the CPV plane and the shower coordinate in the PHOS across magnetic field, B=0.2 T.

4.4.2 Charged shower suppression in the PHOS

Photons in relativistic heavy ion collisions are accompanied by a large number of charged particles which produced an essential background in the PHOS. To match charged particle showers in the PHOS the Charged Particle Veto detector was proposed. For shower matching the coordinates of charged particle hits in the CPV should be projected in the PHOS and compared with coordinates of the showers in the PHOS. If the reconstructed shower in the PHOS is accompanied by a charged track in the CPV, this shower can be produced or distorted by charged particle hit. Such showers should be rejected therefore from the sample of genuine photon showers in the PHOS at the stage of physical analysis of events.

A detailed Monte Carlo studies have been performed to determine the efficiency of the CPV to select genuine photons in the PHOS. To produce a real event, the event generator SHAKER [8] was used. The charged particle density per unit rapidity was taken to be $dN/dy = 8000$, events contained $\pi^0, \pi^\pm, K^\pm, p^\pm$. The events were tracked through the real detector medium by the GALICE package, the correspondent signals in the CPV and PHOS were simulated and reconstructed. As a result, the array of the shower coordinates in the PHOS and array of the hit coordinates in the CPV were obtained for each event.

For each reconstructed shower in the PHOS, the distance from the shower coordinate to the closest reconstructed hit of the charged particle in the PHOS was found. The reconstruction of the charged particle hit in the PHOS can be performed by the extrapolation of the charged track from the reconstructed hit in the CPV. Using the CPV as a stand-alone device, such an extrapolation can be made assuming that the track comes from the beam interaction point. This assumption defines the direction of the track which produced a hit in the CPV, and thus, a coordinate of the hit on the PHOS. Figs. 32 and 33 show the distance from the shower coordinate to the closest charged particle hit on the PHOS along the Z- and Y-axes, using this extrapolation. In the Fig.32 there is a single peak near $\min \Delta Z = 0$ which corresponds to the PHOS showers caused by the charged particles. The PHOS showers not correlated with the charged tracks give the wide background on this plot. Along the Y-axis, the influence of the magnetic field on the charged
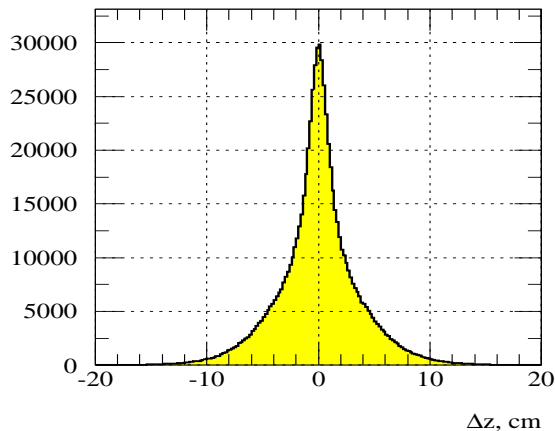
Figure 32: Distance of the shower coordinate to the closest charged track in the PHOS along Z-axis. Track is assumed to come from the interaction point.
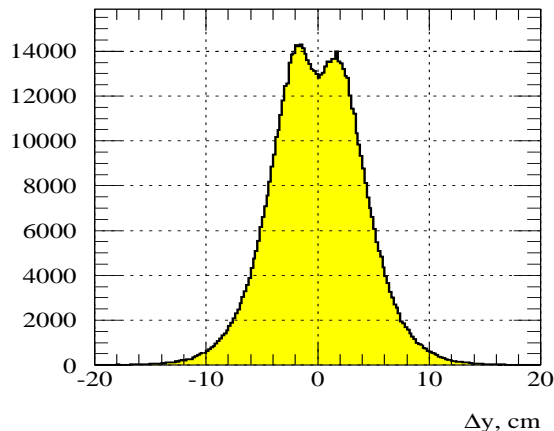
Figure 33: Same as Fig.32 but for the Y-axes.

particles results in the shift between the PHOS shower from the charged particle and the corresponded CPV hit. This effect is seen as two peaks in the Fig.33, left one comes from the positive particles and the right one from the negative particles.

The information from the TPC can be used to define the direction of tracks coming to the CPV more precisely. The extrapolation of the CPV hit to the PHOS using this direction gives a more narrow distribution of the deviation of PHOS shower from the charged track coordinate along the Y-axis which is shown in Fig.4.4.2.
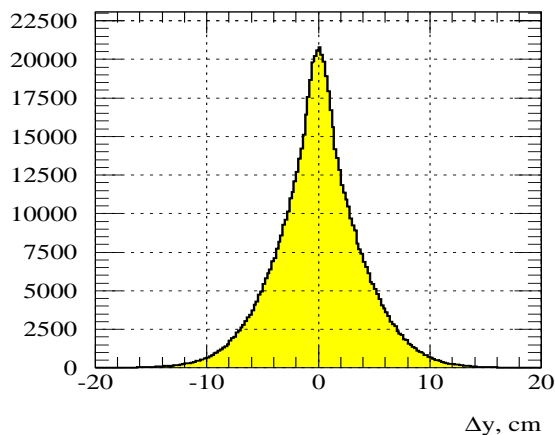

Figure 34: Distance from the PHOS shower coordinate to the closest charged track in CPV along the Y-axis. Track direction is used from the TPC.

These distributions give the criterium of the photon isolation in the PHOS. The reconstructed shower in the PHOS not accompanied by a charged track hit closer than ΔZ_0 ($\min |\Delta Z| > \Delta Z_0$) along the Z-axis and along the Y-axis closer than ΔY_0 ($\min |\Delta Y| > \Delta Y_0$) is determined as an isolated shower, and caused by the photon. The numerical values of ΔZ_0 and ΔY_0 are defined from Figs.32 and 4.4.2. The value of ΔY_0 is energy dependent because soft charged particles are bended more from the straight trajectory on their path from the CPV to the PHOS than particles with higher momenta. The choice of the ΔZ_0 value is not influenced by the particle momentum. In the table 5 the values of ΔY_0 and ΔZ_0 are given for three ranges of the closest PHOS shower momentum.

p, GeV/c	ΔY_0, cm	ΔZ_0, cm
< 0.5	2.8	1.5
$0.5 - 1.0$	2.2	1.5
> 1.0	1.8	1.5

Table 5: Numerical values of ΔY_0 and ΔZ_0.

4.4.3 Independent tuning of the photon isolation parameters

The parameters of the genuine photon isolation in the PHOS discussed above were fixed on the basis of CPV matching accuracy of the charged particles in the PHOS. An independent tuning of these parameters can be performed also by using of physical distributions of photons which can be distorted by misidentified charged hadron showers.

Below we consider the tuning procedure based on the combinatorial mass distribution of photon pairs in the PHOS. For simplicity we use the photon isolation criterion

$$\frac{\Delta Z^2}{\Delta Z_0^2} + \frac{\Delta Y^2}{(\Delta Z_0 + 0.3 cm)^2} > 1 \tag{19}$$

which does not depend on the charged particle momentum. The value $0.3 cm$ takes into account the asymmetry in precision of the charged particle coordinates along and across the ALICE magnetic field. Thus the only free parameter in (19) is ΔZ_0.
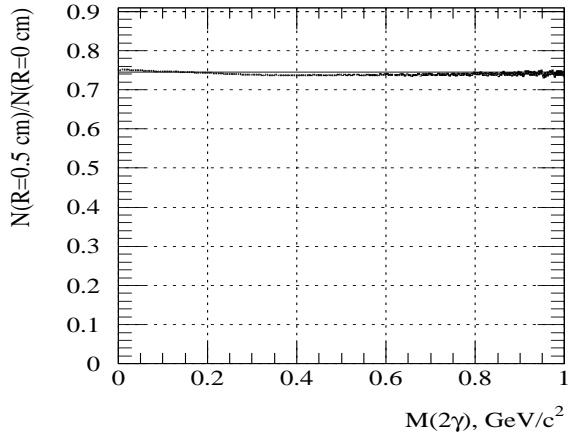

Figure 35: Ratio $R(\Delta Z_0 + 0.5 cm/\Delta Z_0)$ for $\Delta Z_0 = 0$ cm, solid line is a fitted constant, $\chi^2/N_{dof} = 33.5$
.

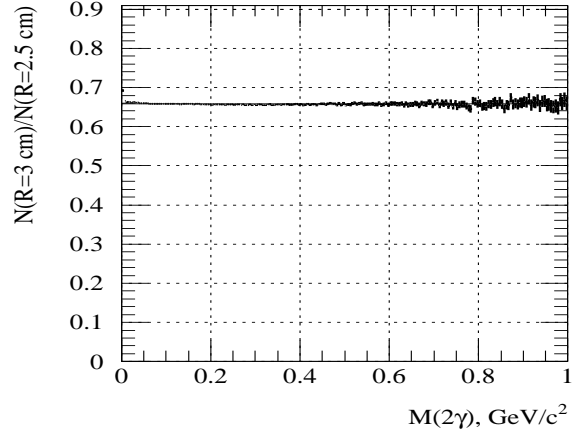Figure 36: Ratio $R(\Delta Z_0 + 0.5 cm/\Delta Z_0)$ for $\Delta Z_0 = 2.5$ cm, solid line is a fitted constant, $\chi^2/N_{dof} = 1.9$

The series of the combinatorial mass distributions of photon pairs (which satisfy (19)) was calculated for different values of the ΔZ_0 parameter: 0., 0.5, 1.0, 1.5, 2.0, 2.5 and 3.0 cm. And the distribution ratios for neighboring parameter values

$$R(\Delta Z_0 + 0.5 cm/\Delta Z_0) = \frac{dN/dM_{\gamma\gamma}(\Delta Z_0 + 0.5 cm)}{dN/dM_{\gamma\gamma}(\Delta Z_0)}. \tag{20}$$

were obtained and fitted with a constant.

If both samples of photons selected for neighboring parameter values, ΔZ_0 and $\Delta Z_0 + 0.5 cm$, contain only genuine photons the ratio R should be a constant because

the ratio can not depend on an accidental suppression of the photons. But if the ratio is not a constant, this means that at least one sample contains showers from charged particles. This criterion can be used to choose the optimal value ΔZ_0 for charged particle suppression in the PHOS. In Fig. 35 and 36 ratios (20) are shown for $\Delta Z_0 = 0\ cm$ and $\Delta Z_0 = 2.5\ cm$, the distribution fits by constants gives the values of χ^2/N_{dof} equal to 33.5 and 1.9 respectively. Thus the value $\Delta Z_0 = 2.5\ cm$ can be considered as the optimal for suppression of the charged showers in the PHOS for isolation criterion (19). The value of ΔZ_0 found is in good agreement with the parameters in Table 5 that means that the criteria are selfconsistent.

4.4.4 Photon reconstruction efficiency

Figs.37 and 38 show the ratios of p_T-spectra of the reconstructed to the generated photons without and with the charged track rejection. From the Fig. 37 it follows that the
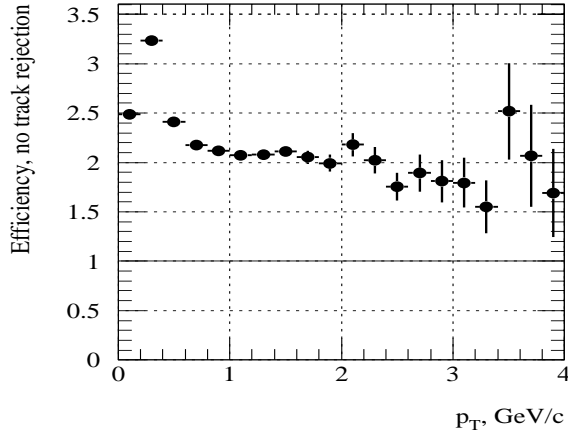

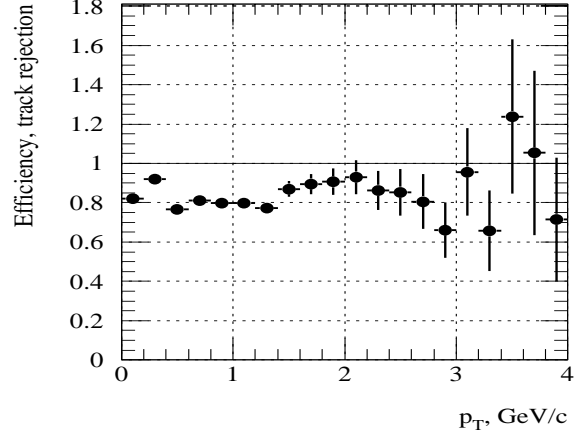Figure 37: Ratio of p_T-spectra without charged track rejection.

Figure 38: Ratio of p_T-spectra with charged track rejection.

number of reconstructed showers in the PHOS is about twice higher, and for small momenta, up to three times higher than the real number of photons hitting the PHOS. This double load of the PHOS is caused by hadrons. After selecting the genuine photon showers in the PHOS, the number of reconstructed photons achieved the level of ~80% compared with the generated one, due to partial photon conversion and CPV rejection. Thus, the Charged Particle Veto detector provide an effective tool to select genuine photons in the PHOS.

References

[1] ALICE Collaboration, High Momentum PID TDR, ALICE TDR 1, CERN/LHCC 98-19, 1998.

[2] P.Le Coultre, L3 a new tool for cosmic ray muon research, Durban Conference, 1997.

[3] A.A.Lednev, NIM A366 (1995) 292.

[4] I.Enddo, T.Kawamoto, Y.Mizuno et al., Nuclear Instruments and Methods 188 (1981) 51-58.

[5] H.Buchholz, Elektrise und magnetische Potentialfelder, Springer (1957).

[6] ALICE Internal Note /98-23.

[7] LeCroy Nuclear Products Catalog.

[8] N. van Eindhoven et al., ALICE internal note 95-32.